

Fluid trajectory evaluation based on an ensemble-averaged cross-correlation in time-resolved PIV

Young Jin Jeon · Ludovic Chatellier ·
Laurent David

Received: 19 December 2013 / Revised: 3 June 2014 / Accepted: 6 June 2014 / Published online: 19 June 2014
© Springer-Verlag Berlin Heidelberg 2014

Abstract A novel multi-frame particle image velocimetry (PIV) method, able to evaluate a fluid trajectory by means of an ensemble-averaged cross-correlation, is introduced. The method integrates the advantages of the state-of-art time-resolved PIV (TR-PIV) methods to further enhance both robustness and dynamic range. The fluid trajectory follows a polynomial model with a prescribed order. A set of polynomial coefficients, which maximizes the ensemble-averaged cross-correlation value across the frames, is regarded as the most appropriate solution. To achieve a convergence of the trajectory in terms of polynomial coefficients, an ensemble-averaged cross-correlation map is constructed by sampling cross-correlation values near the predictor trajectory with respect to an imposed change of each polynomial coefficient. A relation between the given change and corresponding cross-correlation maps, which could be calculated from the ordinary cross-correlation, is derived. A disagreement between computational domain and corresponding physical domain is compensated by introducing the Jacobian matrix based on the image deformation scheme in accordance with the trajectory. An increased cost of the convergence calculation, associated with the nonlinearity of the fluid trajectory, is moderated by means of a V-cycle iteration. To validate enhancements of the present method, quantitative

comparisons with the state-of-arts TR-PIV methods, e.g., the adaptive temporal interval, the multi-frame pyramid correlation and the fluid trajectory correlation, were carried out by using synthetically generated particle image sequences. The performances of the tested methods are discussed in algorithmic terms. A high-rate TR-PIV experiment of a flow over an airfoil demonstrates the effectiveness of the present method. It is shown that the present method is capable of reducing random errors in both velocity and material acceleration while suppressing spurious temporal fluctuations due to measurement noise.

List of symbols

\mathbf{a}	Set of polynomial coefficients, $\mathbf{a} = \{\mathbf{a}_1, \dots, \mathbf{a}_p\}$
\mathbf{a}_k	k th-order polynomial coefficient
$\Delta \mathbf{a}$	Set of corrections vectors for \mathbf{a} , $\Delta \mathbf{a} = \{\Delta \mathbf{a}_1, \dots, \Delta \mathbf{a}_p\}$
$\Delta \mathbf{a}_k$	Corrections vectors for \mathbf{a}_k
$C_n(\Gamma(\mathbf{x}, n))$	Cross-correlation value between two time steps 0 and n along a trajectory
C_{ens}	Ensemble-averaged cross-correlation value
c_n	Contribution of a temporal interval n to bias error
$D\mathbf{u}/Dt$	Material acceleration
$I_n(\mathbf{x})$	Particle image plane at a time step n
$I_n^{\Gamma(\mathbf{x}, n)}$	Deformed particle image by $\Gamma(\mathbf{x}, n)$
$\mathbf{J}(\Gamma(\mathbf{x}, n))$	Jacobian matrix of a deformed image scheme by $\Gamma(\mathbf{x}, n)$
M	Number of images
N_c	Number of averaged cross-correlation maps
n	Normalized times step, $n = t/\Delta t$
n_{opt}	Optimal separation
P	Polynomial order of a modeled trajectory

Y. J. Jeon (✉) · L. Chatellier · L. David
Institut P PRIME, UPR3346, CNRS – Université de Poitiers –
ISAE-ENSMA, 11 Boulevard Marie et Pierre Curie,
86962 Futuroscope Cedex, France
e-mail: young.jin.jeon@univ-poitiers.fr

L. Chatellier
e-mail: ludovic.chatellier@univ-poitiers.fr

L. David
e-mail: laurent.david@univ-poitiers.fr

$R(\Delta \mathbf{a})$	Cross-correlation map for an entire correction of \mathbf{a}
$R_k(\Delta \mathbf{a}_k)$	Cross-correlation map for an individual correction of \mathbf{a}_k
$R_n^{\Gamma(\mathbf{x},n)}(\Delta \mathbf{x})$	Cross-correlation map between I_0 and $I_n^{\Gamma(\mathbf{x},n)}$
Δs	Scale of sampling step for a discrete construction of $R_k(\Delta \mathbf{a}_k)$
Δs_{cri}	Criterion for a scale of sampling step
T	Normalized maximum temporal interval
Δt	Temporal separation between two subsequent recordings
\mathbf{u}	Velocity
u	Exact horizontal displacement
W	Interrogation window
w	Window size
\mathbf{x}	Position in a particle image plane
\mathbf{x}_p	Position of fluid parcel
$\Delta \mathbf{x}$	Coordinate of a computed cross-correlation map
$\Delta \mathbf{x}_{\text{phy}}$	Physical vector which corresponds to $\Delta \mathbf{x}$
β, σ	Bias and random errors
β_1, σ_1	Basis error profiles from numerical assessment
β_n, σ_n	Analytic errors from two-frame cross-correlation with an imposed interval $n, n > 1$
$\beta_{\text{FTC}}, \sigma_{\text{FTC}}$	Analytic errors of the FTC method
β^+, σ^+	Error profiles based on forward deformation scheme
$\delta x, \delta y$	Grid spacings in horizontal and vertical directions
γ	Scale factor of V-cycle iteration
$\Gamma(\mathbf{x}, n)$	Relative fluid trajectory to \mathbf{x}
Γ'	Regulated trajectory field
$\Gamma'_{\pm \delta x}, \Gamma'_{\pm \delta y}$	Regulated trajectories at neighboring grid points
ε	Signed random error

1 Introduction

In recent years, time-resolved particle image velocimetry (TR-PIV) has emerged from an interest in unsteady and turbulent flows that need to be examined in the time or frequency domain. To fulfill the temporal requirement, a high-speed imaging system which generally consists of CMOS cameras in combination with a diode-pumped Nd:YLF laser or continuous-wave laser system is essential to most time-resolved cases (Hain and Kähler 2007). Images recorded by CMOS sensors have low quality and less resolution due to the low sensitivity and high noise level compared to CCD sensors (Litwiller 2001). The

weaker illumination due to the high laser repetition further compounds the problem. Therefore, the subsequent analysis inevitably suffers from lower image quality (Hain et al. 2007; Stanislas et al. 2005). Multiple image sequences, on the other hand, are capable of offering various sets of meaningful cross-correlations, and thereby, there exists a possibility of making up for the loss due to the low image quality. Furthermore, time-related properties can be revealed in concert with the chronologic particle images.

One of the significant discussions in TR-PIV in the literature concerns the improvement of measurement accuracy for the purpose of providing instantaneous data for the analysis of unsteady pressure gradient (Liu and Katz 2006; Kurtulus et al. 2007; Haigermoser 2009; Charonko et al. 2010; Violato et al. 2011; van Oudheusden 2013). Since the measurement uncertainty attendant upon the low image quality could be compensated by using multiple images, several practical procedures have been established by the previous studies as follows:

Concept 1 Optimal temporal separation.

Concept 2 Averaged cross-correlation.

Concept 3 Lagrangian fluid trajectory.

The selection of a proper temporal interval between consecutive recordings, Δt , is required to design PIV experiments in terms of the dynamic range (Boillot and Prasad 1996; Adrian 1997). In turbulent flows, there is an appropriate range of Δt that guarantees relatively low random fluctuations compared to the measurement uncertainty with the acceptable out-of-plane loss (Poelma et al. 2006; Adrian and Westerweel 2010). However, the universal selection of Δt regarding the maximum displacement intensifies the unreliability at extremely small displacement regions such as viscous sublayers and turbulent streaks (Hain and Kähler 2007). To rectify this problem with multi-frame PIV, the locally adaptive selection of optimal interval, $\Delta t_{\text{opt}} = n_{\text{opt}} \Delta t$, has been applied (Pereira et al. 2004; Druon et al. 2006; Hain and Kähler 2007; Persoons and O'Donovan 2010). Hain and Kähler (2007) have offered practical guidelines to select n_{opt} by taking into account both peak quality and flow acceleration. Recently, the guidelines have been further refined by Sciacchitano et al. (2012), based on the ensemble-averaged cross-correlation.

A reduction in random error by averaging data has been applied to PIV in the way of averaging cross-correlation maps (Delnoij et al. 1999; Meinhart et al. 2000; Billy et al. 2004; Scarano et al. 2010). Samarage et al. (2012) have suggested that the hybrid averaging method that utilizes both cross-correlation maps and peak positions. Since the optimized temporal interval could be regarded as a valid temporal range for averaging under a nonstationary flow

condition, Sciacchitano et al. (2012) have proposed the multi-frame pyramid correlation by introducing the ensemble-averaged cross-correlation together with the homothetic transform while also extending the averaging concept into multiple temporal separations, i.e., $n = 1 \dots n_{opt}$.

A prescribed function as the Lagrangian fluid trajectory has been implemented in multi-frame particle tracking velocimetry (PTV) during the past two decades (Malik et al. 1993; Guezennec et al. 1994; Li et al. 2008; Cierpka et al. 2013). Recently, the trajectory of fluid parcels in an interrogation window has been accounted for by the fluid trajectory correlation (FTC) method (Lynch and Scarano 2013), which obtains a fluid trajectory from cross-correlation peaks by means of a least-square fit. The FTC method is able to extend the temporal interval significantly until the deformed particle image collapses under very high deformation at a considerably long temporal interval.

As van Oudheusden (2013) reviews, the ways of using multi-frame particle image sequences can be classified according to how a material acceleration term is evaluated (Violato et al. 2011; de Kat and van Oudheusden 2012). The Navier–Stokes equation under incompressible flow conditions is given as a relation between the pressure gradient and the velocity information:

$$\nabla p = -\rho \frac{D\mathbf{u}}{Dt} + \mu \nabla^2 \mathbf{u}.$$

where the material acceleration $D\mathbf{u}/Dt$ is expressed by the Eulerian and the Lagrangian perspectives, respectively:

$$\frac{D\mathbf{u}}{Dt} = \begin{cases} \frac{\partial \mathbf{u}}{\partial t} + (\mathbf{u} \cdot \nabla) \mathbf{u} & \text{(Eulerian perspective)} \\ \frac{d\mathbf{u}(\mathbf{x}_p(t), t)}{dt} = \frac{d^2 \mathbf{x}_p(t)}{dt^2} & \text{(Lagrangian perspective)} \end{cases},$$

where \mathbf{u} is the velocity and \mathbf{x}_p is the position of the fluid parcel. Figure 1 schematically illustrates both perspectives on a multi-frame image sequence. In the Eulerian perspective, $D\mathbf{u}/Dt$ should be obtained from local and convective accelerations with respect to a stationary reference frame (i.e., each interrogation grid point) due to its time invariant nature. On the contrary, $D\mathbf{u}/Dt$ could be obtained by taking the second derivative of the trajectory function, $\mathbf{x}_p(t)$, in the Lagrangian perspective.

To date, an integration of the optimal temporal separation and the averaged cross-correlation, consistent in the Eulerian perspective, has been accomplished by the multi-frame pyramid correlation method (Sciacchitano et al. 2012). Here, the ensemble-averaged cross-correlation map from different temporal intervals shows great performances in terms of both random and bias errors, but these improvements are limited due to curved and accelerated flow motions, e.g., the multi-frame pyramid

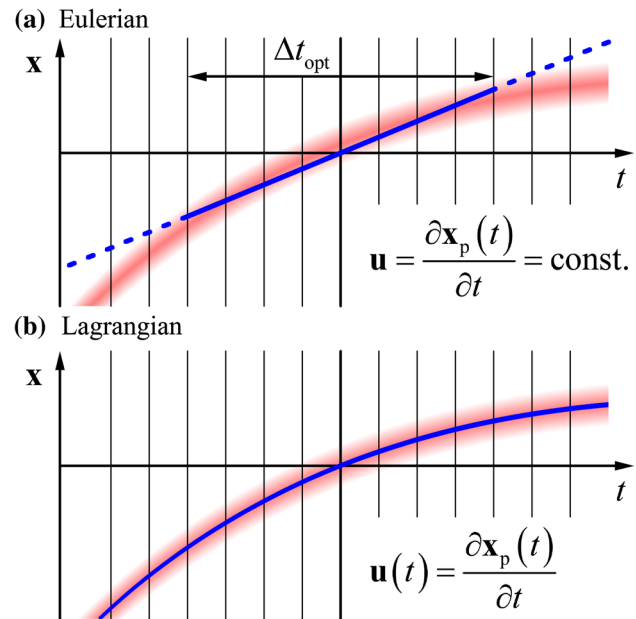


Fig. 1 Perspectives on the multi-frame PIV. **a** Eulerian. **b** Lagrangian. Blue lines indicate obtained velocity and trajectory, while red coded regions show probability distributions of real trajectories

correlation is identical to the two-frame correlation when the optimal interval, n_{opt} , is selected as one due to strong flow acceleration or curved flow motion. As a method to overcome this limitation, an integration of the Lagrangian fluid trajectory onto the averaged cross-correlation might be an alternative approach. Although it is impractical due to the inconsistency in the perspectives, several clues to conjugate both perspectives are already contained in the previous studies. These will be described at the beginning of Sect. 2.

The present study proposes a novel TR-PIV method, namely the fluid trajectory evaluation based on an ensemble-averaged cross-correlation (FTEE), capable of obtaining the most appropriate fluid trajectory based on the ensemble-averaged cross-correlation. Therefore, the solution of the present method is a Lagrangian trajectory, which implies both velocity and material acceleration. The procedure of the present method was induced from relations among the curved trajectory, cross-correlation maps and corresponding physical meanings. Thereby, the practical averaging method along the modeled trajectory has been introduced. To analyze improvements of the present method in terms of algorithmic features, the state-of-the-art TR-PIV methods were also tested by means of synthetic image sequences, and the corresponding improvements were discussed. A high-rate PIV experiment for a flow around an airfoil was conducted in order to assess the spatial and temporal performances of the methods.

2 Algorithm

The present study started from an investigation of the previous methods to integrate the ideas from different perspectives. As with the FTC, the principal basis of the present method (FTEE) was the trajectory evaluation because of its self-consistent feature, e.g., velocity, acceleration and coextensive temporal ranges over an entire image plane. The FTC obtains a fluid trajectory from peak locations of cross-correlation maps by means of a least-square fit, as shown in Fig. 2b. In addition, the FTC has proposed the rotating corrector that compensates the disparity between the computational peak and its actual position, and thus, the method eliminates the oscillation in the iterative correction. By expanding this idea from a correlation peak point into a planar or volumetric map, the cross-correlation map, transformed in accordance with the physical domain, could be regarded as a probability distribution of the fluid trajectory as demonstrated in Fig. 2c. It means that the cross-correlation values surrounding the peak points and the ensemble-averaged cross-correlation along the trajectory, slightly aside from the peaks, are made available. Thus, the present study relies on the assumption that the ensemble-averaged cross-correlation value along the trajectory has the maximum value when the trajectory is the most appropriate.

2.1 Ensemble-averaged cross-correlation value along a trajectory

In the present method, an odd number, $M = 2T + 1$ with the positive integer T , of successive images was employed to evaluate the fluid trajectory with respect to the central time step based on a following polynomial model:

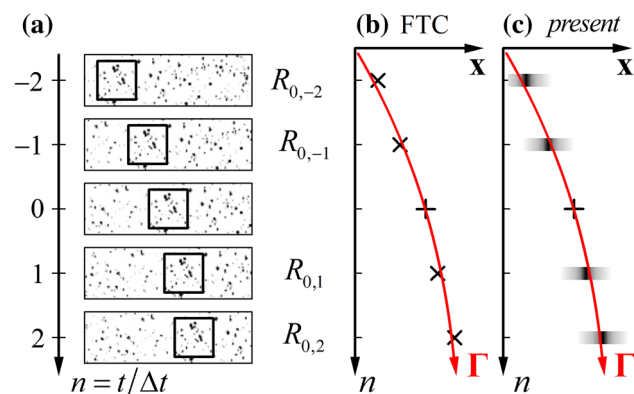


Fig. 2 Relations between a trajectory and cross-correlation maps. **a** Image sequence, **b** FTC, **c** present method (FTEE). Interrogation windows are presented as *black squares*, while $R_{0,n}$ is assumed as 1D cross-correlation map between two time steps 0 and n . Peaks of $R_{0,n}$ are plotted as *times symbol* marks, while $R_{0,n}$ is shown as *gray-scaled* map

$$\mathbf{x}_p(\mathbf{x}, n) = \mathbf{x} + \mathbf{\Gamma}(\mathbf{x}, n), \quad \text{where } \mathbf{\Gamma}(\mathbf{x}, n) = \sum_{q=1}^P \mathbf{a}_q(\mathbf{x})n^q, \tag{1}$$

where $n = t/\Delta t$ is the normalized time step, Δt is the temporal interval between two subsequent recordings, and $\mathbf{x}_p(\mathbf{x}, n)$ is the position of fluid parcel defined for all time steps from $n = -T$ to $+T$, notably $\mathbf{x}_p(\mathbf{x}, 0) = \mathbf{x}$. $\mathbf{\Gamma}(\mathbf{x}, n)$ is the relative fluid trajectory to \mathbf{x} while P is the polynomial order and \mathbf{a}_q is the q th-order polynomial coefficient. Note that \mathbf{x} is the position vector in the particle image plane at $n = 0$. The cross-correlation value between two time steps 0 and n along the trajectory, $C_n(\mathbf{\Gamma}(\mathbf{x}, n))$, can be expressed as following:

$$C_n(\mathbf{\Gamma}(\mathbf{x}, n)) = \int_{W_0} I_0(\mathbf{x})I_n(\mathbf{x} + \mathbf{\Gamma}(\mathbf{x}, n))d\mathbf{x} \tag{2}$$

where $n = -T \dots T$,

where $I_n(\mathbf{x})$ is the particle image plane at the time step n , and W_0 is the interrogation window with respect to $I_0(\mathbf{x})$. Note that a mean intensity of the interrogation window was subtracted from the image intensities in order to obtain a normalized cross-correlation. Finally, the ensemble-averaged cross-correlation value, C_{ens} , is defined as:

$$C_{\text{ens}}(\mathbf{a}(\mathbf{x})) = \frac{1}{2T} \sum_{n=-T}^{n=+T} C_n(\mathbf{\Gamma}(\mathbf{x}, n)), \tag{3}$$

where $\mathbf{a}(\mathbf{x})$ is the set of polynomial coefficients, and $C_0(\mathbf{\Gamma}(\mathbf{x}, 0))$ is neglected as 0 for a meaningful averaging. Then, the set of polynomial coefficients which maximizes C_{ens} can be regarded as the most appropriate solution.

2.2 Strategies for achieving an efficient convergence

Even though Eq. 3 is a simple expression, the construction of the ensemble-averaged map for the correction significantly augments the computational cost because all of the polynomial coefficients must be considered simultaneously:

$$R(\Delta\mathbf{a}) = C_{\text{ens}}(\mathbf{a}(\mathbf{x}) + \Delta\mathbf{a}) = \frac{1}{2T} \sum_{n=-T}^{n=+T} \int_{W_0} I_0(\mathbf{x})I_n\left(\mathbf{x} + \mathbf{\Gamma}(\mathbf{x}, n) + \sum_{q=1}^P \Delta\mathbf{a}_q n^q\right) d\mathbf{x} \tag{4}$$

where $R(\Delta\mathbf{a})$ denotes the ensemble-averaged map defined by $\Delta\mathbf{a}$, the set of polynomial coefficients for the correction, i.e., $\Delta\mathbf{a} = \{\Delta\mathbf{a}_1, \dots, \Delta\mathbf{a}_P\}$. This implies that the coefficients are coupled to each other; therefore, the cross-correlation map should be defined in the entire dimension of $\Delta\mathbf{a}$. To economize on the computational

cost, the present method has adopted the V-cycle convergence method (Braess and Hackbusch 1983) and the homothetic transform of cross-correlation map (Sciacchitano et al. 2012).

The coefficient correction based on the V-cycle was applied in order to correct each coefficient individually. To take into account the relation between the coefficients, each coefficient was sequentially considered by following a low-high-low order, e.g., $1 \rightarrow 2 \rightarrow \dots \rightarrow P \rightarrow P - 1 \rightarrow \dots \rightarrow 1$. Equation 4 can then be uncoupled into

$$R_k(\Delta \mathbf{a}_k) = \frac{1}{2T} \sum_{n=-T}^{n=+T} \int_{W_0} I_0(\mathbf{x}) I_n(\mathbf{x} + \Gamma(\mathbf{x}, n) + \Delta \mathbf{a}_k n^k) \, d\mathbf{x}, \tag{5}$$

where $\Delta \mathbf{a}_k$ is the correction vector of the k th-order polynomial coefficient. Then, the problem can be simplified, e.g., from one 6D map to three 2D maps in the case of 2D PIV with $P = 3$. In contrast to the explicit methods such as the least-square fit, the present method makes a gradual convergence into the appropriate solution.

The homothetic transform of the cross-correlation map is capable of providing $R_k(\Delta \mathbf{a}_k)$ by utilizing one cross-correlation map, i.e., $R_1(\Delta \mathbf{a}_1)$. As the coupled map is no longer necessary owing to the V-cycle correction, the ensemble-averaged cross-correlation maps about the whole polynomial coefficients can be constructed by a single cross-correlation calculation and subsequent homothetic transforms. This will be further discussed in Sects. 2.4 and 2.5.

2.3 Integration with the image deformation

The images were deformed iteratively (Huang et al. 1993; Jambunathan et al. 1995; Scarano and Riethmuller 2000) according to the trajectories, $\Gamma(\mathbf{x}, n)$, by:

$$I_n^{\Gamma(\mathbf{x}, n)}(\mathbf{x}) = I_n(\mathbf{x} + \Gamma(\mathbf{x}, n)), \tag{6}$$

where $I_n^{\Gamma(\mathbf{x}, n)}$ denotes the deformed image by $\Gamma(\mathbf{x}, n)$. Then, the cross-correlation map between the reference image I_0 and the deformed image $I_n^{\Gamma(\mathbf{x}, n)}$ is computed by:

$$R_n^{\Gamma(\mathbf{x}, n)}(\Delta \mathbf{x}) = \int_{W_0} I_0(\mathbf{x}) I_n^{\Gamma(\mathbf{x}, n)}(\mathbf{x} + \Delta \mathbf{x}) \, d\mathbf{x}, \tag{7}$$

where $\Delta \mathbf{x}$ is the coordinate of the computed cross-correlation map, and therefore, $R_n^{\Gamma(\mathbf{x}, n)}$ is obtained with respect to the discrete pixel coordinate $\Delta \mathbf{x}$. Equation 7, after the substitution of Eq. 6 and the application of Taylor expansion under the assumption that $\|\Delta \mathbf{x}\|$ is sufficiently smaller than the window size, becomes.

$$\begin{aligned} R_n^{\Gamma(\mathbf{x}, n)}(\Delta \mathbf{x}) &= \int_{W_0} I_0(\mathbf{x}) I_n(\mathbf{x} + \Delta \mathbf{x} + \Gamma(\mathbf{x} + \Delta \mathbf{x}, n)) \, d\mathbf{x} \\ &= \int_{W_0} I_0(\mathbf{x}) I_n(\mathbf{x} + \Gamma(\mathbf{x}, n) + J(\Gamma(\mathbf{x}, n)) \Delta \mathbf{x}) \, d\mathbf{x}, \end{aligned} \tag{8}$$

where \mathbf{J} denotes the Jacobian matrix of the deformed image scheme (Mayer 2002; Miozzi 2004; Kitchofer et al. 2011; Jeon and Sung 2011). The physical vector $\Delta \mathbf{x}_{\text{phy}}$, which corresponds to $\Delta \mathbf{x}$, is introduced to Eq. 2 so that.

$$C_n(\Gamma(\mathbf{x}, n) + \Delta \mathbf{x}_{\text{phy}}) = R_n^{\Gamma(\mathbf{x}, n)}(\Delta \mathbf{x}) \tag{9}$$

where $\Delta \mathbf{x}_{\text{phy}} = \mathbf{J}(\Gamma(\mathbf{x}, n)) \Delta \mathbf{x}$.

This is schematically represented in Fig. 3, where the physical locations of the original and deformed particle image schemes are illustrated in Fig. 3a while the vectors in computational and physical domains are demonstrated in Fig. 3b, c, respectively. Equation 9 relates the coordinate transformation of the cross-correlation map between the computational domain (RHS) and the physical domain (LHS). Therefore, the individual correction of each polynomial coefficient is now feasible by utilizing the conventional PIV image deformation approach.

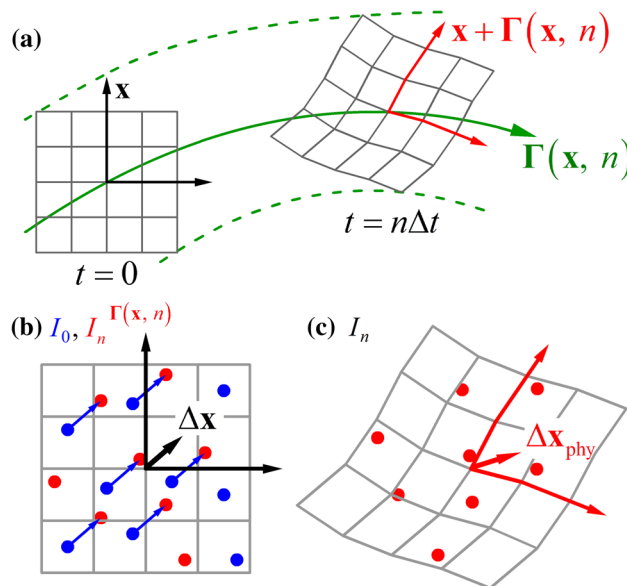


Fig. 3 a Deformed particle image scheme in accordance with trajectories. b, c Coordinate transform between a computation domain (black) and a physical domain (red). Blue and red particles indicate particles in I_0 and I_n , respectively. Solid green line represents a trajectory, which passes through an interrogating grid point at $t = 0$, while dashed green lines show neighboring trajectories

2.4 Corrections of polynomial coefficients

As mentioned earlier, the correction of trajectory was conducted in each polynomial coefficient independently by means of the V-cycle. For the given change of $\Delta \mathbf{a}_k$, Eq. 9 can be rewritten as:

$$C_n(\Gamma(\mathbf{x}, n) + \Delta \mathbf{a}_k n^k) = R_n^{\Gamma(\mathbf{x}, n)} \left(\mathbf{J}(\Gamma(\mathbf{x}, n))^{-1} \Delta \mathbf{a}_k n^k \right). \tag{10}$$

Recalling Eq. 5, the correction of the k th-order polynomial coefficient can be then performed by:

$$R_k(\Delta \mathbf{a}_k) = \frac{1}{2T} \sum_{n=-T}^{n=+T} R_n^{\Gamma(\mathbf{x}, n)} \left(\mathbf{J}(\Gamma(\mathbf{x}, n))^{-1} \Delta \mathbf{a}_k n^k \right). \tag{11}$$

Note that Eq. 11 is identical to the homothetic transformation introduced by the pyramid correlation method (Sciacchitano et al. 2012) under the condition of $\mathbf{J} = \mathbf{I}$. The cross-correlation value for the given change of $\Delta \mathbf{a}_k$ was interpolated from the pixelated cross-correlation map, $R_n^{\Gamma(\mathbf{x}, n)}$, by applying the bicubic interpolation scheme (Astarita and Cardone 2005; Sciacchitano et al. 2012). The cross-correlation map of $R_k(\Delta \mathbf{a}_k)$ was then constructed by changing $\Delta \mathbf{a}_k$ stepwise from the origin to neighboring points.

Figure 4 demonstrates the procedure of the coefficient correction, Eq. 11. The squares indicate the cross-correlation maps, which are transformed in accordance with the physical plane while their color gradients inside the squares represent cross-correlation values. Errors in the x -direction only are represented, whose values are exaggerated in order to clearly show the procedure. The homothetic transform of each cross-correlation map is shown in Fig. 4c, while Fig. 4b, c shows how the cross-correlation values are ensemble-averaged in order to correct the first-order

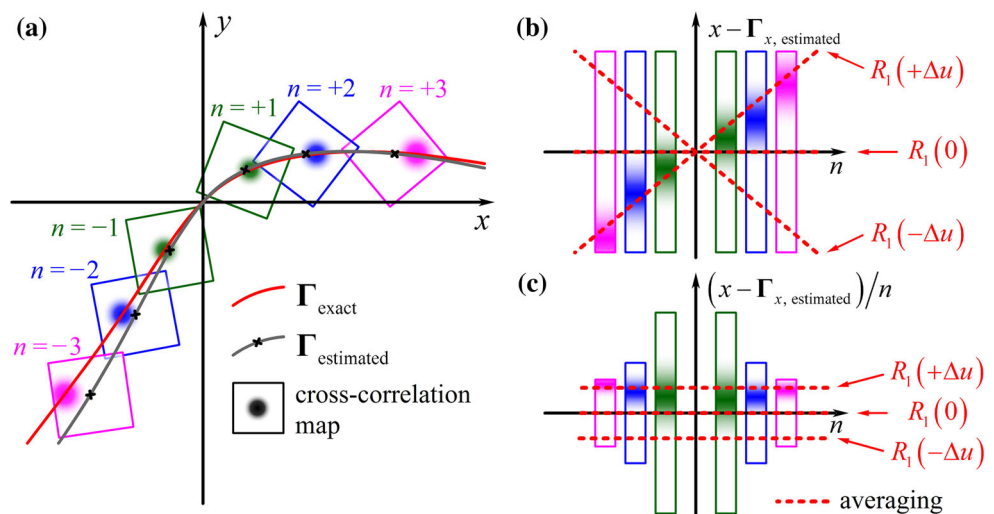
polynomial coefficient. This homothetic relation can also be expanded into higher-order polynomial coefficients.

2.5 Practical procedures

When dealing with a curved trajectory, attention should be paid to stability in order to trigger the V-cycle correction. The present method starts from the shortest trajectory and extends it by adopting the pseudo-tracking procedure (Jensen et al. 2003; Liu and Katz 2006) at both tails. In extending the trajectory, the polynomial order should be less than M in order to avoid under-determination of the system, e.g., the polynomial order should be one or two when $M = 3$.

After each pseudo-extension of the trajectory is completed, it is delivered into the iterative correction procedure. Each correction procedure consists of one image deformation and multiple V-cycle iterations. Once the particle image sequence is deformed with respect to the current trajectory, the V-cycle corrections are performed iteratively by decreasing the scale of the sampling step Δs , while $R_k(\Delta \mathbf{a}_k)$ is discretely sampled. To match the scale of Δs as one pixel at the trajectory edges, Δs is initially set as $1/T^k$ pixels and decreased by a factor γ , where $0.5 \leq \gamma < 1$, when one V-cycle correction is over. In the present method, $\gamma = 0.5$ was used. The V-cycle correction terminates when Δs is smaller than the prescribed criterion Δs_{cri} . Until the expansion is completed, the accuracy of the trajectory is not a critical matter if the approximate trajectory is known. Thus, the number of iterations, equal to the number of image deformations, at the extension stage could be reduced to < 5 , and the convergence criterion Δs_{cri} could be set as a large value such as 0.1 pixels. At the final stage of the complete trajectory evaluation, the iteration number and Δs_{cri} should be newly set, e.g., 15 and $\Delta s_{\text{cri}} < 10^{-4}$.

Fig. 4 Demonstration of coefficient correction. **a** Transformed cross-correlation maps (squares) based on estimated trajectory (black), **b**, **c** correction of horizontal velocity Δu . Dashed red lines denote averaging processes



The Jacobian matrices are set prior to the image deformation at the beginning of each iterative correction procedure. Since the image deformation generally needs the predictor correction in the interest of stable convergence (Nogueira et al. 1999; Lecuona et al. 2002; Schrijer and Scarano 2008), the trajectory is regulated by using the neighboring trajectories. The Jacobian matrix at each grid point is then evaluated based on the regulated trajectory by referring neighboring grid points in the central difference scheme (Raffel et al. 1998). In the case of a 2D system, \mathbf{J} can be expressed as:

$$\mathbf{J}(\mathbf{\Gamma}'(\mathbf{x}, n)) = \begin{bmatrix} \frac{2\delta x + \mathbf{\Gamma}'_{+\delta x} - \mathbf{\Gamma}'_{-\delta x}}{2\delta x} & \frac{\mathbf{\Gamma}'_{+\delta x} - \mathbf{\Gamma}'_{-\delta x}}{2\delta y} \\ \frac{\mathbf{\Gamma}'_{+\delta y} - \mathbf{\Gamma}'_{-\delta y}}{2\delta x} & \frac{2\delta y + \mathbf{\Gamma}'_{+\delta y} - \mathbf{\Gamma}'_{-\delta y}}{2\delta y} \end{bmatrix}, \tag{12}$$

wherein $\mathbf{\Gamma}'$ denotes the regulated trajectory field, while δx and δy denote the grid spacings in horizontal and vertical directions, and $\mathbf{\Gamma}'_{\pm\delta x}$, $\mathbf{\Gamma}'_{\pm\delta y}$ are corresponding neighboring trajectories.

3 Numerical assessment

3.1 Synthetic image sequences and computational parameters

Two image sequences including translation and rotation were synthetically generated for quantitative evaluations, following Adrian (1984), Raffel et al. (1998) and Lecordier and Westerweel (2004). The image sequence with uniform horizontal displacements u from 0 to 2 pixels was prepared in order to compare the present algorithm with others, that is, two-frame cross-correlation with an imposed interval (Hain and Kähler 2007), sliding averaging method (Meinhart et al. 2000; Scarano et al. 2010), pyramid correlation method (Sciaccitano et al. 2012) and FTC (Lynch and Scarano 2013). Note that the iterative image deformation (Scarano and Riethmuller 2000) was applied in every test case. Figure 5 presents computational characteristics of each algorithm. The image sequence with rigid rotation from 0° to 90° was also generated using 5° steps. In the case of the rigid rotation, only the FTC and the present method (FTEE) were tested due to the limitations on the optimal time separation under the curved flow motion. The particles were randomly distributed over an image plane of $1,024 \times 1,024$ (translation) and 300×300 (rotation) pixels, respectively, with a uniform seeding density of 0.1 particles/pixel. The particle diameter was uniformly set as 1.414 pixels. The final interrogation window was set as 15×15 pixels with 75 % overlap (4×4 pixels spacing)

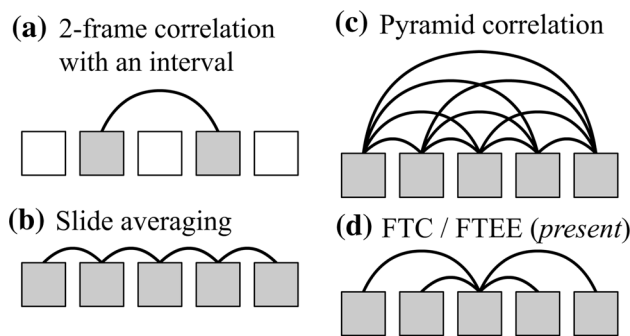


Fig. 5 Tested algorithms. *Square boxes* indicate single images, and images used in each analysis are filled with *gray* while arcs mean cross-correlations

with Gaussian weighting (Astarita 2007). The interpolation scheme for the image deformation, the sinc interpolation scheme (Scarano and Riethmuller 2000), with 8×8 pixel kernel was applied. The material accelerations of the methods in the Eulerian perspectives and the trajectory-based methods with $P = 1$ were computed by referring neighboring velocities with a backward temporal scheme. All TR-PIV methods mentioned in the present study along with the synthetic image generator were coded in C++ using the SLIP library of Institut PPRIME and XLIM (Tremblais et al. 2010).

3.2 Effects of the temporal interval and the averaged cross-correlation

The effect of the normalized temporal interval n is presented in Fig. 6a. Here, the bias error β and the random error σ are defined for evaluation as:

$$\beta(u) = \langle u \rangle - u$$

$$\sigma(u) = \sqrt{\frac{1}{N_{\text{data}}} \sum_{i=1}^{N_{\text{data}}} (\langle u \rangle - u_i)^2} \quad \text{where } \langle u \rangle = \frac{1}{N_{\text{data}}} \sum_{i=1}^{N_{\text{data}}} u_i, \tag{13}$$

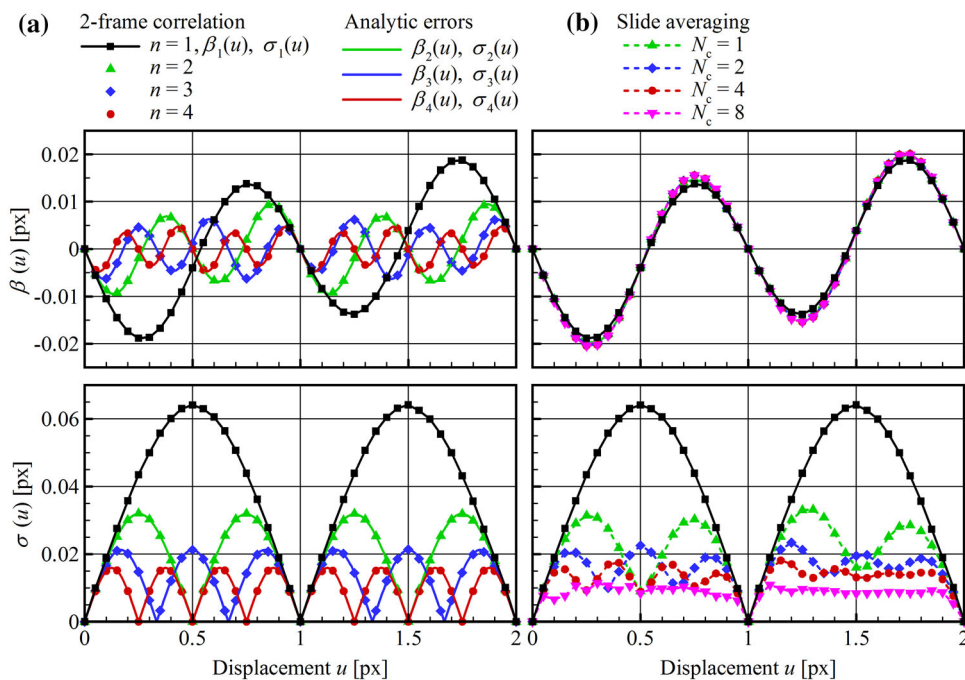
where u_i and u are the measured and exact horizontal displacements, respectively, while N_{data} indicates the number of measured points. Since the results have homothetic relation with respect to $1/n$, the analytic errors with the imposed temporal interval n , β_n and σ_n , were introduced as:

$$\beta_n(u) = \frac{1}{n} \beta_1(nu) \quad \text{where } \beta_1(u) = \beta_1(u + 2) \tag{14a}$$

and

$$\sigma_n(u) = \frac{1}{n} \sigma_1(nu) \quad \text{where } \sigma_1(u) = \sigma_1(u + 1), \tag{14b}$$

Fig. 6 a Results of two-frame correlation with an imposed interval n while analytic errors refer the Eqs. 14a and 14b. **b** Results of sliding averaging with respect to a number of averaged cross-correlation maps, N_c , while *solid black* lines are identical to $\beta_1(u)$ and $\sigma_1(u)$



where the result when $n = 1$ is regarded as the basis error profiles through β_1 and σ_1 . Note that the period of β_1 is two pixels due to the symmetric image deformation scheme.

Figure 6b provides the effect of the averaged cross-correlation where N_c denotes the number of averaged cross-correlation maps. Since the temporal interval of each cross-correlation is identical, the bias errors show similar profiles with slightly increased magnitudes. As shown in Fig. 7, approximately 10 % increased bias errors were obtained with respect to the case of single cross-correlation. By sacrificing small amounts of bias error, the averaged cross-correlation achieved significantly reduced random errors. In cases of small u and N_c , the trend of the random error looks similar to Fig. 6a regardless of the approach, i.e., increasing n or N_c . But this trend disappears for larger u and N_c , and the general feature of averaging is shown. This could be explained in terms of a shared image pattern and its averaging effect. The averaging of cross-correlation maps was performed at the stationary grid point, and thus, each cross-correlation map shared specific portion of image pattern with the adjacent maps, e.g., $(1 - u/w)/w$, where w is the window size. The consecutive cross-correlations were highly coherent due to large amount of the sharing portion, and thereby, effects of one biased image pattern could affect two cross-correlation maps with opposite directions. Therefore, the biased cross-correlation maps could be compensated by each other. It is the reason why the random errors have local minimums at $u = 1/N_c$. As u or N_c increased, the coherency between each cross-

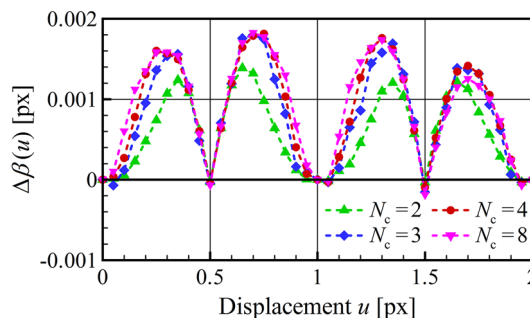


Fig. 7 Increment in bias error $\Delta\beta$ due to the averaged cross-correlation. $\Delta\beta$ is calculated from: $\Delta\beta = \text{sgn}(\beta_1) \cdot (\beta_{N_c} - \beta_1)$

correlation disappeared and the averaging effect was strengthened.

3.3 Multi-frame pyramid correlation

The bias and random errors of the multi-frame pyramid correlation are shown in Fig. 8. Note that T , in the pyramid correlation, represents the normalized maximum temporal interval, i.e., $T = M - 1$. The overall trends follow the two-frame cross-correlation under the same T , i.e., $\beta_T(u)$ and $\sigma_T(u)$ from Eq. 14a, but they show improved results. Since the cross-correlation maps from different temporal intervals are ensemble-averaged, a contribution of each temporal interval on the resulting bias error, c_n , could be quantified by using the following formula:

Fig. 8 Results of the multi-frame pyramid correlation in comparison with the two-frame correlation

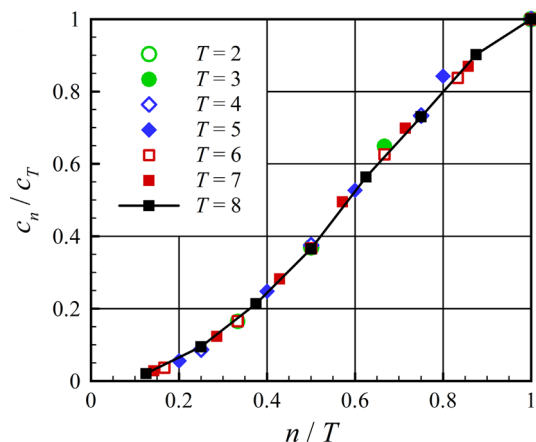
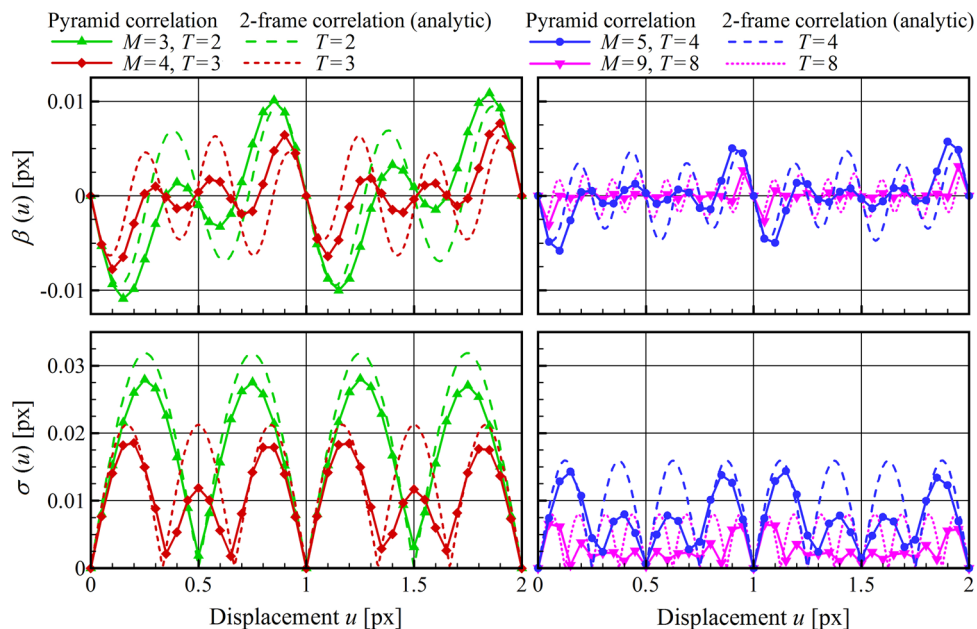


Fig. 9 Normalized contribution coefficients c_n/c_T with respect to n/T for the multi-frame pyramid correlation

$$\beta_{PYR,T}(u) \approx \sum_{n=1}^T c_n \beta_n(u) = \sum_{n=1}^T c_n \left\{ \frac{1}{n} \beta_1(nu) \right\}, \quad (15)$$

where $\sum_{n=1}^T c_n = 1$.

where β_{PYR} denotes the bias error of the pyramid correlation method. The contribution coefficients, c_n , were evaluated in the least-square manner by sampling $\beta_1(u)$ from every 0.05 pixel displacement. Figure 9 shows the plots of normalized contribution coefficients c_n/c_T , which show the specific trend irrespective of T . It means that the minor temporal intervals, i.e., 1 to $T - 1$, can affect the final result with specific portions. Since the combination of

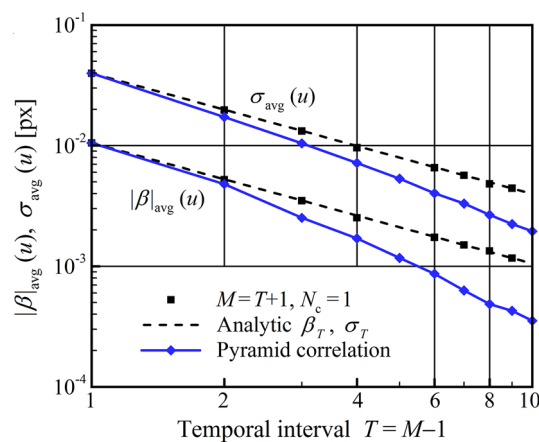


Fig. 10 Reductions in averaged errors of the multi-frame pyramid correlation as a temporal interval T increases (blue); black symbols represent the results from the two-frame analysis, while dashed lines indicate analytic estimates

oscillating profiles from various frequencies is able to reduce overall magnitude, the mean fluctuations $|\beta|_{avg}$ and σ_{avg} , averaged between $u = 0$ and 2 pixels, rapidly decrease as T increases in comparison with the cases of single cross-correlation as shown in Fig. 10. In contrast, the pixel-locking effect is intensified in comparison with β_T due to the influences of the minor temporal intervals, i.e., $\beta_1 - \beta_{T-1}$. In the perspective of the random error, the pyramid correlation method also shows an improved performance. However, how the ensemble-averaged cross-correlation from different time separations reduces the random error is still unknown, and further analysis is necessary in order to reveal the theoretical mechanism.

3.4 Trajectory-based methods, FTC and FTEE

The FTC and the present method (fluid trajectory evaluation based on an ensemble-averaged cross-correlation—FTEE) acquire the trajectories by the use of an identical set of cross-correlation maps. The only difference between FTC and FTEE is the method used to acquire the trajectory, i.e., the least-square fitting and the ensemble-averaged cross-correlation. This implies that the bias error profiles of both methods should be identical but not the random error profiles. Although both methods are able to reduce the random error, the mechanisms influencing the random error seem to be dissimilar. For the FTC method, the randomness of each cross-correlation map may affect the cross-correlation peaks and the subsequent least-square fit. This means that the influence of relatively large errors is significant. In contrast, the FTEE method is capable of excluding the relatively large errors. This is the underlying principle of the FTEE method, and thereby, a reduced random error is expected compared to the FTC.

Since the FTC utilizes the least-square fitting, the bias error profile, β_{FTC} , can be analytically obtained from the following:

$$\begin{bmatrix} \beta_1^+(-Tu) \\ \vdots \\ \beta_1^+(Tu) \end{bmatrix} = \begin{bmatrix} -T & \cdots & (-T)^P \\ \vdots & & \vdots \\ T & \cdots & T^P \end{bmatrix} \begin{bmatrix} \beta_{FTC,T}(u) \\ \vdots \\ \beta_{FTC,T}(a_p) \end{bmatrix}, \tag{16}$$

where T represents the normalized maximum temporal intervals of cross-correlations, i.e., $T = (M - 1)/2$. β^+ and σ^+ denote the error profiles based on the forward deformation scheme and have also homothetic relations similar to Eqs. 14a and 14b.

$$\beta_n^+(u) = \frac{1}{n} \beta_n^+(nu) \quad \text{where } \beta_1^+(u) = \beta_1^+(u + 1) \tag{17a}$$

and

$$\sigma_n^+(u) = \frac{1}{n} \sigma_1^+(nu), \quad \text{where } \sigma_1^+(u) = \sigma_1^+(u + 1). \tag{17b}$$

Note that the period of β_1^+ is now one pixel because of the forward deformation scheme. Then, the solutions for $P = 1, 2, 3$ and 4 are derived as:

$$\beta_{FTC,T,P=1\text{or}2}(u) = \frac{\sum_{n=1}^T n \beta_1^+(nu)}{\sum_{n=1}^T n^2} \tag{18a}$$

and

$$\begin{aligned} \beta_{FTC,T,P=3\text{or}4}(u) &= \frac{\sum_{n=1}^T n^4 \cdot \sum_{n=1}^T n^3 \beta_1^+(nu) \cdot \sum_{n=1}^T n^6 \cdot \sum_{n=1}^T n \beta_1^+(nu)}{\sum_{n=1}^T n^4 \cdot \sum_{n=1}^T n^4 - \sum_{n=1}^T n^6 \cdot \sum_{n=1}^T n^2}. \end{aligned} \tag{18b}$$

Due to the orthogonality, the analytic solutions of one and two are the same, and likewise for three and four. Comparisons between the FTC, the FTEE and the analytical profiles are shown in Figs. 11 and 12 with good agreement. Here, the basis profile, $\beta_1^+(u)$, was sampled from every 0.05 pixel displacement with the forward image deformation scheme in order to obtain the analytical profiles, $\beta_{FTC}(u)$.

As with the bias error, the random error of the FTC can also be obtained analytically by the use of the basis profile $\sigma_1^+(u)$. In order to take into account a direction of the pixel-locking effect, a signed profile $\varepsilon_n^+(u)$ was introduced:

$$\varepsilon_n^+(u) = \text{sgn}(\beta_n^+(u)) \cdot \sigma_T^+(u). \tag{19}$$

In addition, the coherency between σ_{-n}^+ and σ_{+n}^+ , discussed in the Sect. 3.2, should be also considered. Since the simplest case, when $T = 1$ and $P = 1$ or 2 , was obtained from two cross-correlation maps whose image patterns are identical, the signed random error $\sigma_{FTC,T=1,P=1\text{or}2}$ could be assumed as:

$$\varepsilon_{FTC,T=1,P=1\text{or}2}^+(u) = \frac{1}{2} \varepsilon_1^+(2u). \tag{20}$$

By assuming that the coherent relation can be applied to the cases of $n \geq 2$ and the contribution of each signed random error profile $\varepsilon_n^+(u)$ is identical to the contribution of each bias error profile $\beta_n^+(u)$, the random error profiles read as:

$$\sigma_{FTC,T,P=1\text{or}2}(u) = \left| \frac{\sum_{n=1}^T n \varepsilon_1^+(2nu)}{2 \sum_{n=1}^T n^2} \right| \tag{21a}$$

and

$$\begin{aligned} \sigma_{FTC,T,P=3\text{or}4}(u) &= \left| \frac{\sum_{n=1}^T n^4 \cdot \sum_{n=1}^T n^3 \varepsilon_1^+(2nu) - \sum_{n=1}^T n^6 \cdot \sum_{n=1}^T n \varepsilon_1^+(2nu)}{2(\sum_{n=1}^T n^4 \cdot \sum_{n=1}^T n^4 - \sum_{n=1}^T n^6 \cdot \sum_{n=1}^T n^2)} \right|. \end{aligned} \tag{21b}$$

Figure 11 supports these assumptions in deriving the analytic random error profile of the FTC with good agreement.

The random errors of the FTEE method were about 55 % of the errors of the FTC method under the same conditions of T and P , as shown in Fig. 12, and thereby, this shows that the ensemble-averaged cross-correlation is capable of achieving about 45 % additional random error reduction in comparison with the least-square fitting. The random errors of the FTC and the FTEE methods about the translating and rotating motion are compared in Fig. 13 in terms of the maximum temporal interval. The minimum reductions of random errors about the velocity and the material acceleration are observed as 45 and 46 % for the

Fig. 11 Result of the FTC in comparison with errors analytically obtained by Eqs. 18a and 21a

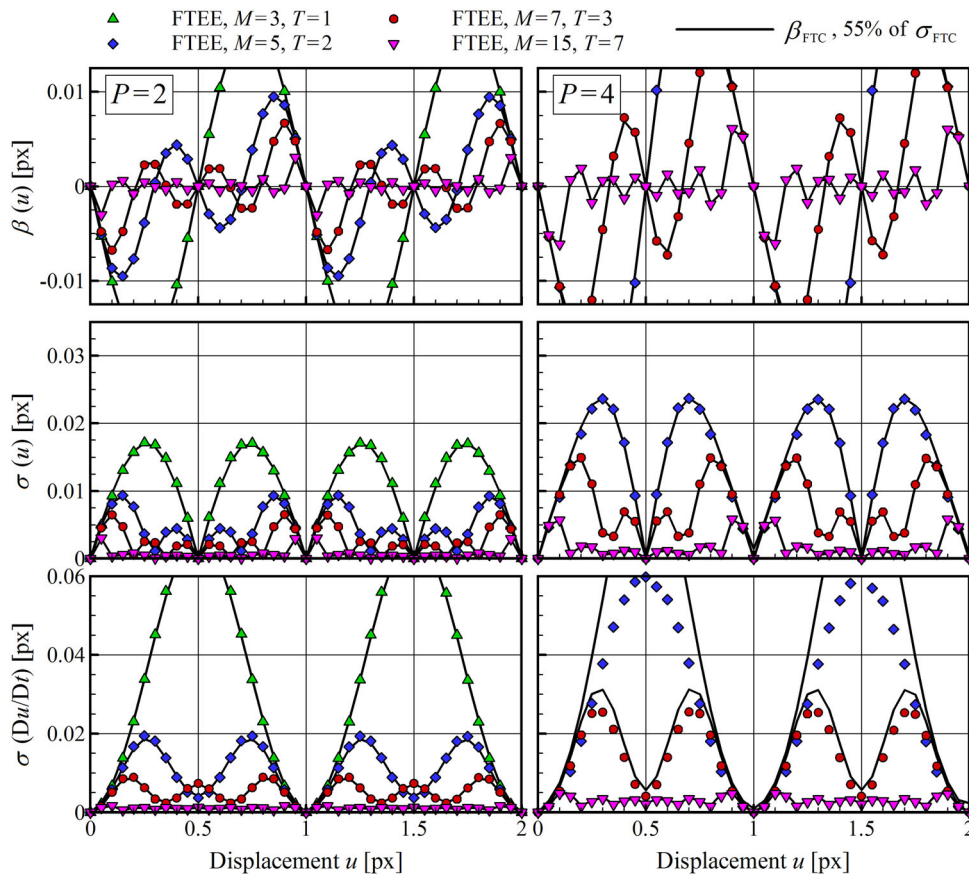
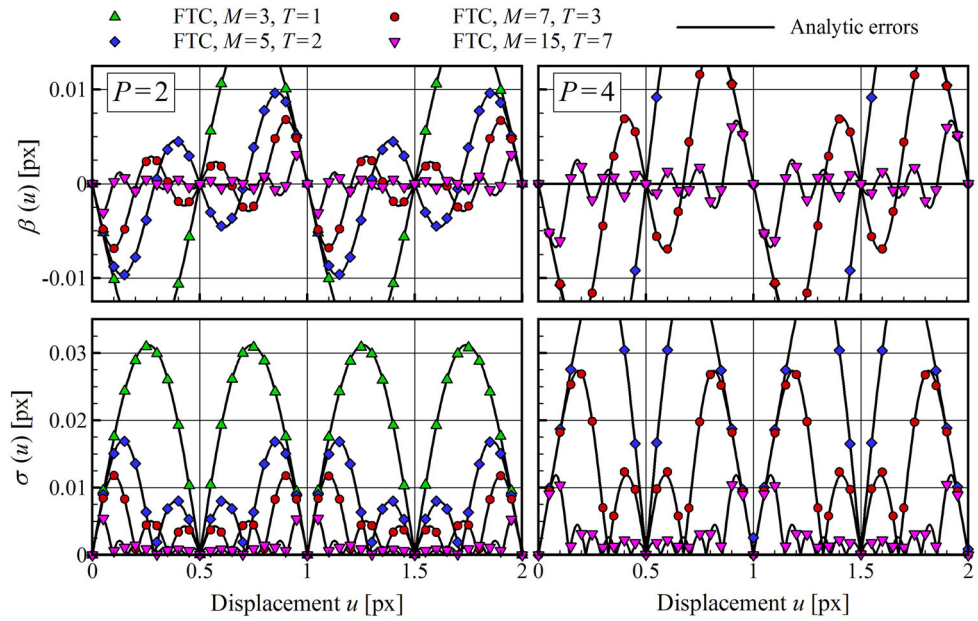
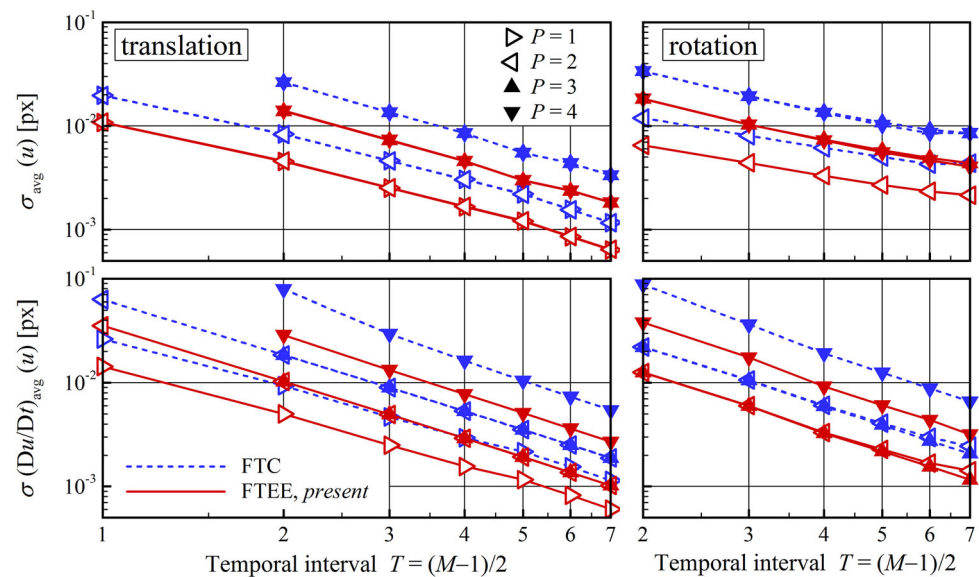


Fig. 12 Result of the present method (FTEE) in comparison with the result of the FTC; for clear comparisons, the random errors of the FTC are scaled by 55 % of the originals

Fig. 13 Comparisons of random errors between the fluid trajectory correlation (*dashed blue lines*, FTC) and the present (*solid red lines*, FTEE)



translation and 46 and 43 % for the rotation, respectively. The random errors of velocity $\sigma(u)$ about $P = X$ and $X + 1$, where X is an odd integer, show identical results due to the orthogonality. On the other hand, the random errors of material acceleration $\sigma(\mathbf{Du}/Dt)$ about $P = X + 1$ and $X + 2$ show identical results due to the differentiation of the trajectory function. The reductions in random errors are observed as a steady ratio, about 45 % of the FTC errors, irrespective of T , P and the flow motions. Therefore, the FTEE method could be universally effective in multi-frame PIV analysis.

4 Experimental assessment

A high-rate measurement of the flow around a NACA0015 airfoil of chord 80 mm with an angle of attack of 30° , slightly oscillating from 28° to 32° , at $Re = 10^5$ has been carried out in order to investigate the validity of the numerical assessments. The image sequence was obtained at a framerate of 1,500 Hz with $1,024 \times 1,024$ pixels resolution. The final interrogation windows were set to 31×31 pixels with 75 % overlapping (8×8 pixels spacing). Figure 14 shows instantaneous velocity contours with contour lines to emphasize the random noise. The multi-frame PIV methods show improved results in comparison with the two-frame correlation shown in Fig. 14a. In the case of the pyramid correlation method, the velocities in the small n_{opt} region were not improved due to the limitation on the number of ensemble-averaged maps (Fig. 14a4). Here, n_{opt} was evaluated by referring the guidelines of the pyramid correlation method. Since the FTC and the FTEE methods account for curved fluid motions with accelerations, the overall velocities show

improved results (Fig. 14b, c). Because the third-order polynomial coefficient could affect the velocity, the results from polynomial orders $P = 2$ and 3 show significant differences. As the number of images M increases, both FTC and FTEE present improved results. Compared to the FTC method, the FTEE method shows improved results with regressed random noise. Figure 14c4 shows contours similar to Fig. 14c3 even though the polynomial order increases.

The effect of the random noise is clearly shown in Fig. 15 in the perspective of instantaneous material acceleration. Note that the error correction process by means of the median filter (Westerweel and Scarano 2005) was applied to the velocity and other polynomial coefficients. Figure 15a4 shows the streamlines while two rotating flow motions exist behind the leading and trailing edges. Since the FTC and the FTEE methods obtain the material acceleration directly while the Eulerian perspective-based methods refer the previous time step, they show more reliable results. The major flow rotation, starting from the trailing edge, is clearly observed with centripetal material accelerations, and the small rotation after the leading edge is also visible. Due to the second-order polynomial coefficient, a half of material acceleration is not closely related to the both first- and third-order polynomials, and the results from different polynomial orders $P = 2$ and 3 had the same random noise levels (Fig. 15b, c).

Figure 16 provides the time histories of the horizontal velocity and the vertical material acceleration. The velocities were sampled at two grid points, indicated as A and B in the sketch encapsulated in Fig. 16b, and the material acceleration was sampled at grid point A only. The methods follow a common trend overtime, while the FTEE has lower

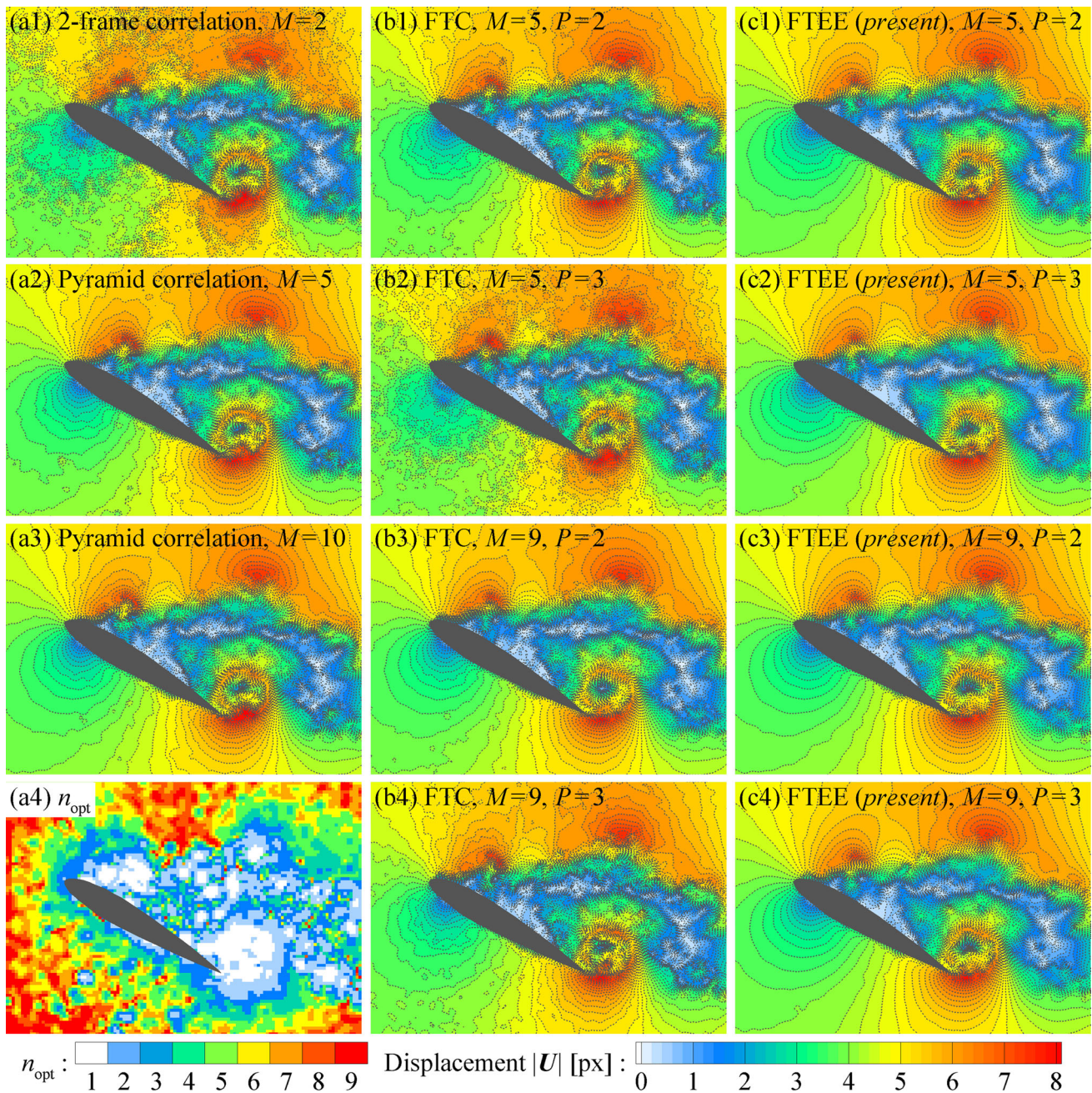


Fig. 14 Instantaneous contours of velocity fields; *contour lines* are plotted every 0.2 pixels velocity magnitude

fluctuating amplitude. As the angle of attack increases until $t = 30$ ms, the horizontal velocity at the point A is accelerated. Meanwhile, a strong rotating flow motion is generated, thereby the vertical material acceleration has positive value. As the angle of attack decreases from $t = 30$ ms, the velocity is saturated for 10 ms while the rotating flow motion is still observed at the point A until $t = 40$ ms. After $t = 40$ ms, meaningful material acceleration is not observed because the center of rotating flow is also moved upward with respect to the location of trailing edge.

5 Conclusion

A novel multi-frame PIV algorithm has been proposed by introducing the FTEE. The technique was designed to obtain ensemble-averaged cross-correlation maps along Lagrangian trajectories. Therefore, the measurement robustness and accuracy have been improved while considering the curved and accelerated fluid motion. The practical procedure has been introduced by deriving the relation between the trajectory and the corresponding

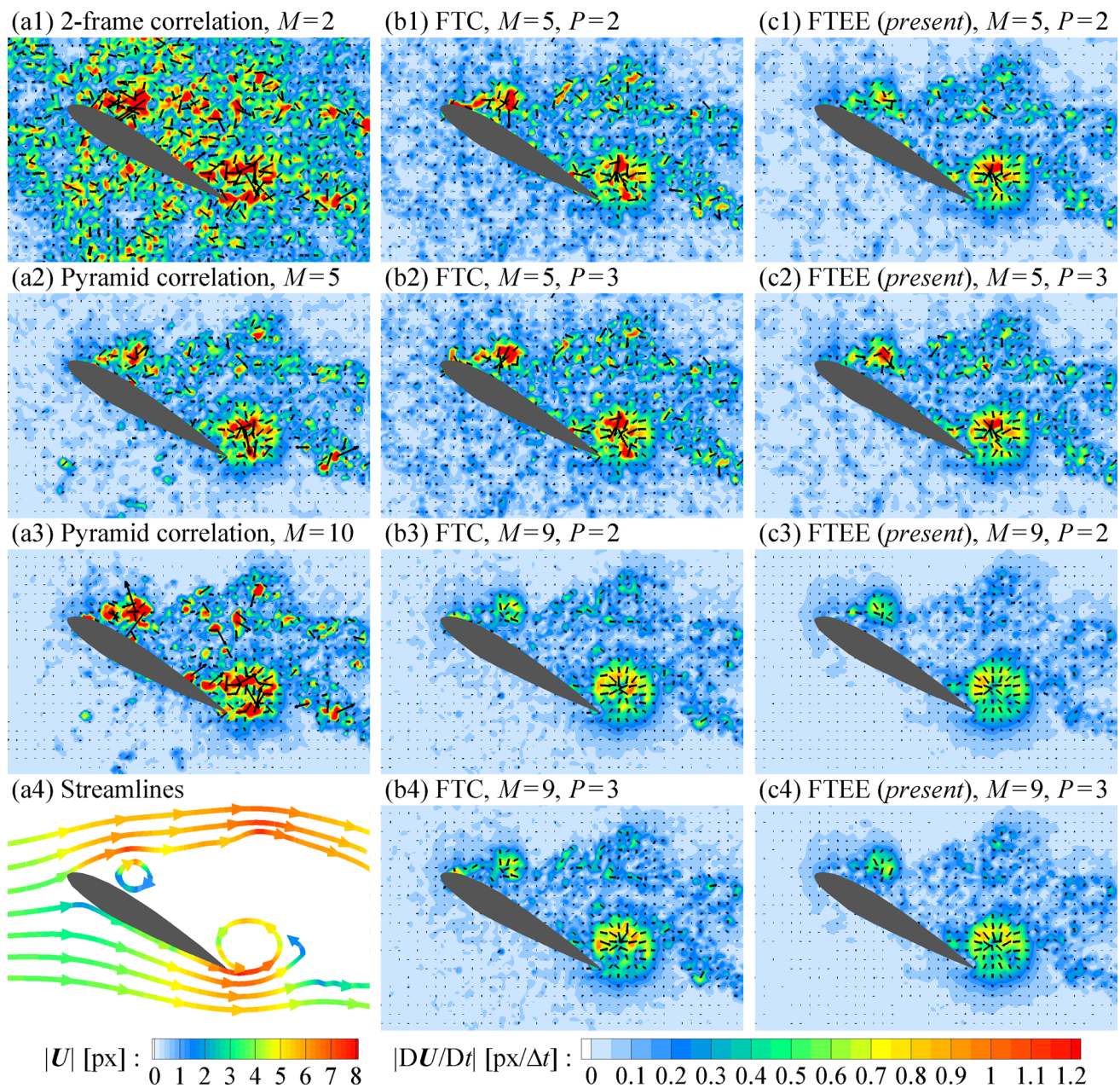


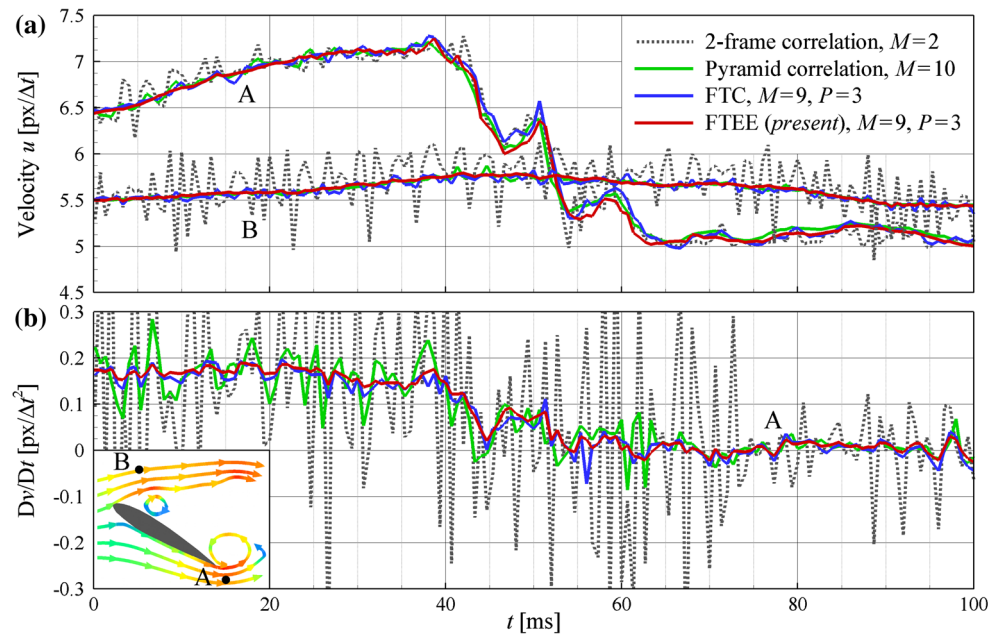
Fig. 15 Instantaneous contours and vectors of material acceleration; vectors are plotted at intervals of three grid steps (i.e., 24 pixels). **a4** Instantaneous streamlines are evaluated from the velocity field from the FTEE when $M = 9$ and $P = 2$

cross-correlation maps in order to both economize on the calculation cost and pursue the simple implementation into the ordinary PIV method. To achieve this, the nonlinearity in obtaining the solution was minimized by introducing the gradual convergence method by means of the V-cycle iteration. The ensemble-averaged cross-correlation map for correcting each polynomial coefficient was constructed by means of the homothetic transformation in relation to the Jacobian matrix regarding the deformed image scheme.

To validate the present approach and prove its applicability, the state-of-the-art TR-PIV methods, the

adaptive temporal interval, the multi-frame pyramid correlation and the FTC were tested and compared. The reason why each method is capable of reducing the errors has been discussed in terms of algorithmic features such as temporal interval, averaged cross-correlation and least-square fitting. The analytic bias error profile of each method was evaluated by taking into account the contributions of various temporal intervals in a good agreement with the numerical assessment. The random error profiles were also investigated theoretically under several assumptions, but further approaches

Fig. 16 Time histories of measured results. **a** Horizontal velocity, **b** vertical material acceleration. One hundred and fifty-one instantaneous fields are shown within 100 ms ($\Delta t = 1/1,500$ s)



in dealing with the averaged cross-correlation might be essential in order to clarify the real mechanism. The present approach achieved steady reductions in the random errors, about 45 %, in both the translating and rotating fluid motion compared to the FTC. Not only the instantaneous velocity and material acceleration fields but also their time histories from high-rate PIV experiment supported the effectiveness of the present approach.

As with the FTC method, the most important feature of the present method (FTEE) was the material acceleration that is obtained with respect to the particle image sequence by means of the modeled trajectory. Both methods kept the framework of iterative image deformation PIV in order to achieve the convergence over the entire particle image. Therefore, the methods were able to exclude a possibility of sudden temporal change while computing the material acceleration in comparison with the methods based on the Eulerian perspective. Furthermore, since the present method has adopted the ensemble-averaged cross-correlation, one could expect greater reduction in random error compared to the FTC. In conclusion, the FTEE method was able to provide reliable displacement and material acceleration with reduced random noise levels for application of subsequent post-processes, such as evaluations of instantaneous pressure fields and fluid dynamic loads.

Acknowledgments The current work has been conducted as part of the AFDAR project, Advanced Flow Diagnostics for Aeronautical research, funded by the European Commission program FP7, Grant No. 265695.

References

- Adrian RJ (1984) Scattering particle characteristics and their effect on pulsed laser measurements of fluid flow: speckle velocimetry vs particle image velocimetry. *Appl Optics* 23:1690–1691
- Adrian RJ (1997) Dynamic ranges of velocity and spatial resolution of particle image velocimetry. *Meas Sci Technol* 8:1393
- Adrian RJ, Westerweel J (2010) Particle image velocimetry. Cambridge University Press, Cambridge
- Astarita T (2007) Analysis of weighting windows for image deformation methods in PIV. *Exp Fluids* 43:859–872
- Astarita T, Cardone G (2005) Analysis of interpolation schemes for image deformation methods in PIV. *Exp Fluids* 38:233–243
- Billy F, David L, Pineau G (2004) Single pixel resolution correlation applied to unsteady flow measurements. *Meas Sci Technol* 15:1039
- Boillot A, Prasad AK (1996) Optimization procedure for pulse separation in cross-correlation PIV. *Exp Fluids* 21:87–93
- Braess D, Hackbusch W (1983) A new convergence proof for the multigrad method including the V-cycle. *SIAM J Numer Anal* 20:967–975
- Charonko JJ, King CV, Smith BL, Vlachos PP (2010) Assessment of pressure field calculations from particle image velocimetry measurements. *Meas Sci Technol* 21:105401
- Cierpka C, Lütke B, Kähler CJ (2013) Higher order multi-frame particle tracking velocimetry. *Exp Fluids* 54:1–12
- De Kat R, Van Oudheusden BW (2012) Instantaneous planar pressure determination from PIV in turbulent flow. *Exp Fluids* 52:1089–1106
- Delnoij E, Westerweel J, Deen NG, Kuipers JAM, Van Swaaij WPM (1999) Ensemble correlation PIV applied to bubble plumes rising in a bubble column. *Chem Eng Sci* 54:5159–5171
- Druon M, Tremblais B, Augereau B, Billy F, David L (2006) Algorithmes pour la vélocimétrie par imagerie de particules résolue dans le temps. In: Congrès Francophone de Techniques Laser, Toulouse, France, 19–22 September 2006, pp 243–252
- Guezennec YG, Brodkey RS, Trigui N, Kent JC (1994) Algorithms for fully automated three-dimensional particle tracking velocimetry. *Exp Fluids* 17:209–219
- Haigermoser C (2009) Application of an acoustic analogy to PIV data from rectangular cavity flows. *Exp Fluids* 47:145–157

- Hain R, Kähler CJ (2007) Fundamentals of multiframe particle image velocimetry (PIV). *Exp Fluids* 42:575–587
- Hain R, Kähler CJ, Tropea C (2007) Comparison of CCD, CMOS and intensified cameras. *Exp Fluids* 42:403–411
- Huang HT, Fiedler HE, Wang JJ (1993) Limitation and improvement of PIV. *Exp Fluids* 15:263–273
- Jambunathan K, Ju XY, Dobbins BN, Ashforth-Frost S (1995) An improved cross correlation technique for particle image velocimetry. *Meas Sci Technol* 6:507
- Jensen A, Pedersen GK, Wood DJ (2003) An experimental study of wave run-up at a steep beach. *J Fluid Mech* 486:161–188
- Jeon YJ, Sung HJ (2011) PIV measurement of flow around an arbitrarily moving body. *Exp Fluids* 50:787–798
- Kitzhofer J, Nonn T, Brücker C (2011) Generation and visualization of volumetric PIV data fields. *Exp Fluids* 51:1471–1492
- Kurtulus DF, Scarano F, David L (2007) Unsteady aerodynamic forces estimation on a square cylinder by TR-PIV. *Exp Fluids* 42:185–196
- Lecondier B, Westerweel J (2004) The EUROPIV synthetic image generator. In: Stanislas M, Westerweel J, Kompenhans J (eds) Particle image velocimetry: recent improvements. Springer, Heidelberg, pp 145–161
- Lecuona A, Nogueira J, Rodríguez P, Santana D (2002) Accuracy and time performance of different schemes of the local field correction PIV technique. *Exp Fluids* 33:743–751
- Li D, Zhang Y, Sun Y, Yan W (2008) A multi-frame particle tracking algorithm robust against input noise. *Meas Sci Technol* 19:105401
- Litwiller D (2001) CCD vs. CMOS. *Photonics Spectra* 35:154–158
- Liu X, Katz J (2006) Instantaneous pressure and material acceleration measurements using a four-exposure PIV system. *Exp Fluids* 41:227–240
- Lynch K, Scarano F (2013) A high-order time-accurate interrogation method for time-resolved PIV. *Meas Sci Technol* 24:035305
- Malik NA, Dracos T, Papantoniou DA (1993) Particle tracking velocimetry in three-dimensional flows. *Exp Fluids* 15:279–294
- Mayer S (2002) A generalized processing technique in digital particle image velocimetry with direct estimation of velocity gradients. *Exp Fluids* 33:443–457
- Meinhart CD, Wereley ST, Santiago JG (2000) A PIV algorithm for estimating time-averaged velocity fields. *J Fluids Eng* 122:285–289
- Miozzi M (2004) Particle image velocimetry using feature tracking and Delaunay tessellation. In: 12th international symposium on applications of laser techniques to fluid mechanics, Lisbon, Portugal
- Nogueira J, Lecuona A, Rodriguez PA (1999) Local field correction PIV: on the increase of accuracy of digital PIV systems. *Exp Fluids* 27:107–116
- Pereira F, Ciarravano A, Romano GP, Di Felice F (2004) Adaptive multi-frame PIV. In: 12th international symposium on applications of laser techniques to fluid mechanics, Lisbon, Portugal
- Persoons T, O'Donovan TS (2010) High dynamic velocity range particle image velocimetry using multiple pulse separation imaging. *Sensors* 11:1–18
- Poelma C, Westerweel J, Ooms G (2006) Turbulence statistics from optical whole-field measurements in particle-laden turbulence. *Exp Fluids* 40:347–363
- Raffel M, Willert CE, Kompenhans J (1998) Particle image velocimetry: a practical guide. Springer, Heidelberg
- Samarage CR, Carberry J, Hourigan K, Fouras A (2012) Optimisation of temporal averaging processes in PIV. *Exp Fluids* 52:617–631
- Scarano F, Riethmuller ML (2000) Advances in iterative multigrad PIV image processing. *Exp Fluids* 29:S051–S060
- Scarano F, Bryon K, Violato D (2010) Time-resolved analysis of circular and chevron jets transition by tomo-PIV. In: 15th international symposium on applications of laser techniques to fluid mechanics, Lisbon, Portugal, 5–8 July 2010
- Schrijer FFJ, Scarano F (2008) Effect of predictor–corrector filtering on the stability and spatial resolution of iterative PIV interrogation. *Exp Fluids* 45:927–941
- Sciacchitano A, Scarano F, Wieneke B (2012) Multi-frame pyramid correlation for time-resolved PIV. *Exp Fluids* 53:1087–1105
- Stanislas M, Okamoto K, Kähler CJ, Westerweel J (2005) Main results of the second international PIV challenge. *Exp Fluids* 39:170–191
- Tremblais B, David L, Arrivault D, Dombre J, Chatellier L, Thomas L (2010) SLIP: simple library for image processing (version 1.0) [software, CeCILL-C Licence]. University of Poitiers, France
- Van Oudheusden BW (2013) PIV-based pressure measurement. *Meas Sci Technol* 24:032001
- Violato D, Moore P, Scarano F (2011) Lagrangian and Eulerian pressure field evaluation of rod-airfoil flow from time-resolved tomographic PIV. *Exp Fluids* 50:1057–1070
- Westerweel J, Scarano F (2005) Universal outlier detection for PIV data. *Exp Fluids* 39:1096–1100